Journal of Materials Chemistry A

Atomic-Level Characterization of Oxygen Storage Material $YBaCo_4O_{7+\delta}$ Synthesized at Low Temperature

Journal:	*Journal of Materials Chemistry A*
Manuscript ID	TA-ART-05-2022-003952.R1
Article Type:	Paper
Date Submitted by the Author:	12-Sep-2022
Complete List of Authors:	Huang, Hsin-Hui; Japan Fine Ceramics Center, Nanostructures Research Laboratory Kobayashi, Shunsuke; Japan Fine Ceramics Center, Nanostructures Research Laboratory Tanabe, Toyokazu; National Defense Academy, Department of Materials Science and Engineering Komiyama, Kaihei; Kanagawa University, Department of Materials and Life Chemistry Saito, Miwa; Kanagawa University, Department of Materials and Life Chemistry Motohashi, Teruki; Kanagawa University, Department of Materials and Life Chemistry Kuwabara, Akihide; Japan Fine Ceramics Center, Nanostructures Research Laboratory

ARTICLE

Atomic-Level Characterization of Oxygen Storage Material $YBaCo_4O_{7+\delta}$ Synthesized at Low Temperature

Received 00th January 20xx,
Accepted 00th January 20xx

DOI: 10.1039/x0xx00000x

Hsin-Hui Huang,*[a] Shunsuke Kobayashi,*[a] Toyokazu Tanabe,[b] Kaihei Komiyama,[c] Miwa Saito,[c] Teruki Motohashi [c] and Akihide Kuwabara [a]

The oxygen storage material, $YBaCo_4O_{7+\delta}$ (YBCO), synthesized at a low temperature of 800 °C, shows extremely fast oxygen absorption/desorption with moderate oxygen storage capacity. Before exploiting the potential use in oxygen-related applications, a comprehensive study of its crystal and electronic structures at the atomic scale is beneficial. Here, using scanning transmission electron microscopy, we find that stacking faults are formed and randomly distributed throughout the particle. Electron energy loss spectroscopy reveals that the surface layer contains a higher oxidation state of cobalt (+3), which is significantly different from the inner part (lower oxidation state of cobalt). Combining observed structural features with the oxygen storage performance, we suggest that structural defects and surface state govern the amount of oxygen that can be stored, while the surface area determines the oxygen absorption/desorption kinetics. This work provides insights into the structure-property relationship, leading to a better understanding of the design of oxide materials with promising oxygen storage properties.

Introduction

Oxygen nonstoichiometry is important for functional oxide materials in the use of broad fields and applications. A group of transition metal oxides containing multivalent cations is known to exhibit oxygen nonstoichiometry. They can store and release oxygen in response to changes in temperature and/or the surrounding atmosphere, and thus be classified as oxygen storage materials (OSMs). The importance of oxygen nonstoichiometry arises from the fact that oxygen content determines the crystal structures, physical properties, and hence the utilization. This unique behavior of OSMs uplifts their potential to be used in automotive three-way catalysts,[1,2] solid-oxide fuel cells,[3] oxygen sensors,[4] and oxygen production (pressure swing absorption),[5,6] *etc*.

$YBaCo_4O_{7+\delta}$ (YBCO) is recognized as a promising candidate exhibiting outstanding oxygen storage capacity (OSC) and excellent oxygen absorb/desorb reversibility.[7,8] This material can store a large amount of oxygen (OSC ≈ 2440 μmol O/g, with $\delta \approx 1.3$) into its crystal structure, substantially exceeding the values reported for conventional oxygen storage materials, such as CeO_2-ZrO_2 (OSC ≈ 1500 μmol O/g).[8–10] The oxygen storage capability could further reach $\delta \approx 1.5$ under specific conditions, which corresponds to the valence of cobalt to be approximately 3.[10,11] Moreover, oxygen absorption/desorption reactions take place reversibly at relatively low temperatures (approximately 400 °C).[10] Such a high tunability of oxygen content at low temperatures has attracted various oxygen-related applications.

The crystal structure of oxygen stoichiometric $YBaCo_4O_7$ is described as hexagonal $P6_3mc$ or trigonal P31c space groups.[12–16] The structural framework consists of two types of corner-sharing CoO_4 tetrahedra, located separately in alternating triangular and Kagomé layers, respectively (see Figs. S1a and S1b). These two types of tetrahedra are distinguished by different bond lengths. Coincidently, the Co^{2+}/Co^{3+} ratio in YBCO is the same as that of the ratio of these two cobalt sites (3:1), however, it might not be directly related to its charge ordering of cobalt sites as predicted by bond valence sum (BVS) calculations.[17] Upon oxygen absorption, the additional oxygen atoms are most likely to bond with some of the tetrahedral cobalt oxides and convert them into octahedra. As a consequence, the overall oxidation state rises, average cobalt valence increases, and the crystal structure changes to an orthorhombic symmetry with a space group of $Pbc2_1$ (see Figs. S1c-f).[18,19] In other words, the amount of oxygen incorporated into the lattice determines the cobalt valence state and the extent of structural changes (see Figs. S1cd and S1ef). As mentioned earlier, the oxygen content can vary in the range of $0 \le \delta \le 1.5$, corresponding to changes in the cobalt valence of 2.25 to 3, which can be expressed in the following formula, $YBaCo^{2+}_{3-2\delta}Co^{3+}_{1+2\delta}O_{7+\delta}$ ($0 \le \delta \le 1.5$). Overall, the open network and flexibility enable tunable structures and oxygen storage performance.

[a] *Nanostructures Research Laboratory, Japan Fine Ceramics Center, 2-4-1 Mutsuno, Atsuta-ku, Nagoya, 456-8587, Japan.*
[b] *Department of Materials Science and Engineering, National Defense Academy, 1-10-20, Hashirimizu, Yokosuka, Kanagawa 239-0811, Japan.*
[c] *Department of Materials and Life Chemistry, Faculty of Engineering, Kanagawa University, 3-27-1 Rokkakubashi, Kanagawa-ku, Yokohama, 221-8686, Japan.*
† *H.-H Huang and *S. Kobayashi are corresponding authors
Electronic Supplementary Information (ESI) available: [details of any supplementary information available should be included here]. See DOI: 10.1039/x0xx00000x

Despite the great deal of attention that YBCO has gained in the last years, much research continues focusing on improving the oxygen storage property.[20,21] For functional materials, the property is generally governed by the size and shape of the particles, and their atomic arrangement, all of which are directly controlled by synthesis methods and conditions. For example, to enhance the oxygen absorption/desorption rate, a small particle size with a high surface area will be ideal. As a ceramic oxide, to obtain a small particle size, the use of low-sintering temperature is subjected to be a better suggestion to avoid grain growth.[22,23] However, to obtain a thermodynamically stable YBCO phase, it is required to sinter at high temperatures of 1000–1200 °C in solid-state reaction synthesis or sol-gel process.[10,12,18,24,25] Pre-treatments, such as ball-milling of the starting powders and preparation of phase-pure powders, are effective in lowering the synthesis temperature to 900–950 °C.[26] Alternatively, post-treatment (ball-milling) on high-temperature synthesized YBCO could directly reduce its particle size down to a few micrometers.[27] Recently, Chen *et al*. reported that YBCO was successfully synthesized at 800 °C by a glycine-complex decomposition method, exhibiting a fast response to oxygen uptake/release.[28] Apart from particle size reduction, low-temperature synthesis or pre/post-treatment might induce crystallographic defects into the structures, and possibly further alter the oxygen storage performance. Thus, a comprehensive understanding of the structural changes in the course of low-temperature firing and the relationship between such structures and oxygen storage property is important, which is still lacking in detail to date.

In this study, we characterize the crystal structure of YBCO synthesized at low temperature (at 800 °C) at atomic resolution by scanning transmission electron microscopy (STEM). Structural disorders such as stacking faults were observed to be randomly distributed without disturbing the overall configuration. In addition, the electron energy-loss spectroscopy (EELS) revealed that the surface region (approximately 40 nm thick) contains cobalt ions with higher valence, which is significantly different from the inner structure. A comparative analysis was also made by examining the YBCO synthesized at the conventional temperature of 1200 °C. We, therefore, establish a connection between the findings from structural characterization to the oxygen storage property.

Results and discussion

X-ray diffraction study

The effect of synthesis temperature on the structure of YBCO was investigated by X-ray diffraction (XRD), as shown in Fig. S2. The high-temperature synthesized YBCO (hereafter named HT-YBCO) has lattice constants of a = 6.3056(3) Å and c = 10.2249(6) Å with the $P6_3mc$ space group. The crystal structure agrees with those reported earlier[12]. In comparison to HT-YBCO, the low-temperature synthesized YBCO (hereafter named LT-YBCO) shows a smaller lattice parameter of a (6.299(2) Å) and a larger lattice parameter of c (10.268(4) Å). The increase in the c lattice parameter of LT-YBCO may be related to its low crystallinity and/or the presence of structural defects.[28] Careful inspection on the XRD pattern of LT-YBCO reveals the peak broadening that might be caused by the presence of defects (discuss later). It should be noted that no extra peak was found in both HT- and LT-YBCOs, indicating no presence of secondary phases or by-products.

Structural analysis by scanning transmission electron microscopy

The effect of synthesis temperature on the particle size and morphology of YBCO was investigated by STEM. Low-magnification HAADF images of HT- and LT-YBCOs are shown in Figs. 1a and 1b, respectively. The micrographs reveal that the HT-YBCO grains are relatively large compared to the LT-YBCO particles. Further, particle size distributions of YBCO were obtained by measuring the size of more than 100 randomly selected particles from several HAADF-STEM images (see Supporting Information, Fig. S3). The average particle size of HT-YBCO is approximately 0.82 ± 0.72 μm, while the LT-YBCO particles show an average size of 0.22 ± 0.13 μm, which is more than three times smaller than HT-YBCO. The difference in particle size can be explained by the firing temperatures. High firing temperature led to grain growth and resulted in the formation of large-size particles. Figure 1c presents a selected area electron diffraction (SAED) pattern of HT-YBCO taken along the a-axis direction. Distinct spots are observed, and the pattern matches well with the simulated results,[12] as shown in the bottom-right corner in Fig. 1c. On the other hand, the SAED pattern of LT-YBCO exhibits diffuse streaks along [0001] direction (as indicated by arrows in the enlarged image at the bottom-right corner in Fig. 1d), suggesting the presence of planar defects such as stacking faults. A high density of bright-line contrasts along the (0001) plane of the YBCO crystal is observed, attributed to the stacking faults. It should be noted

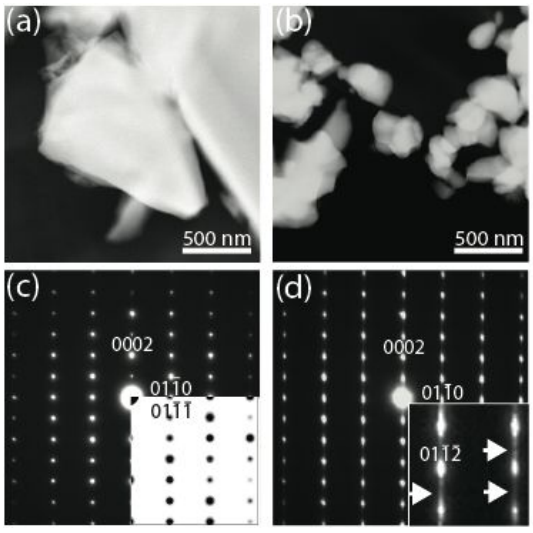

Fig. 1 HAADF-STEM images of (a) HT-YBCO and (b) LT-YBCO. SAED patterns of a single particle oriented to $[2\bar{1}\bar{1}0]$ in (c) HT-YBCO and (d) LT-YBCO. The bottom-right corner in (c) shows the calculated diffraction pattern of $YBaCo_4O_7$. Clear diffuse streaks are shown as indicated by arrows in an enlarged diffraction pattern in (d).

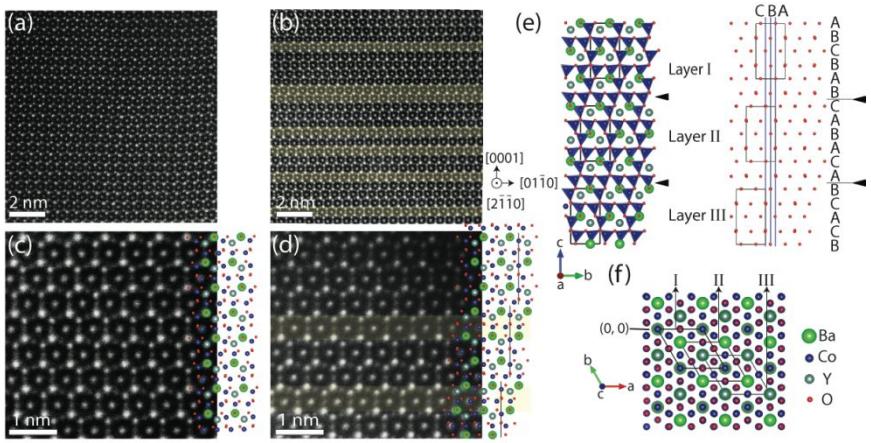

Fig. 2 HAADF-STEM images of the pristine samples of (a) HT-YBCO and (b) LT-YBCO. The yellow highlighted in (b) indicates the position of stacking faults. The magnified HAADF-STEM images of (c) HT-YBCO and (d) LT-YBCO. Schematic atomic arrangements of these samples are partially overlapped on the HAADF-STEM images. Detailed structural configurations and stacking sequences of (d) are illustrated in (e). The constructed illustration viewed along the *c*-axis is shown in (f). The rectangles and rhombuses represent the unit cells of YBCO. Solid arrows indicate the stacking faults planes.

that the streaks are shown only along [0001] direction, which is confirmed by tilting at different orientations (see Fig. S4).

To further elucidate the details of the structure, HT- and LT-YBCOs were taken at atomic resolution by HAADF-STEM imaging, as shown in Fig. 2a and 2b, respectively. As the HAADF-STEM image is so-called Z-contrast image, where the intensity of an atomic column is approximately proportional to the square of the atomic number (Z), the heavier atomic columns appear as brighter spots.[29] Here, the brightness of the spots in the descending order represents the atomic columns of Ba, Y, and Co. The atomic columns of O are practically invisible due to Z^2 dependence and non-optimal imaging conditions.[30] In HT-YBCO, no structural defect (Fig. 2a) is observed. The Ba, Y, and Co atoms, as denoted with different colors, are overlapped on the HAADF image in Fig. 2c. With careful investigation, a breakdown of the stacking sequences along [0001] direction is found in LT-YBCO (Fig. 2b), as highlighted in yellow, indicating the presence of stacking faults. This observation is consistent with the streaks observed on the SAED patterns. Based on the oxygen framework, the stacking sequence of HT-YBCO is labeled as -ABCB- along the *c*-axis, composed of close-packed alternating O_4 and BaO_3 layers. In the region of stacking faults (Figs. 2de), the plane slips along the *b*-axis direction, resulting in a -CABA- stacking sequence and a -BCAC- stacking sequence.

It should be noted that the stacking sequence differs from place to place and is randomly distributed throughout the whole structure. Moreover, the stacking fault density was estimated to be 19.8 % by counting the layer number of stacking faults at different regions (see Fig. S5). This amount of stacking faults attributes to the peak broadening on the XRD patterns of LT-YBCO (Fig. S2). Based on Fig. 2d, plausible structures are drawn by the VESTA program[31] and illustrated in Figs. 2e and 2f. For ease of discussion, three layers separated by stacking faults are labeled as Ⅰ, Ⅱ, and Ⅲ in Fig. 2e. The unit cell of each layer is outlined by a black rectangle. Despite the presence of the stacking faults, no obvious misplacement of the atom from the ideal structure is observed with projected along the *a*-axis and *c*-axis, as shown in Fig. 2e and 2f, respectively. This implies no destruction of the chemical configuration, as the structure is still composed of alternating triangular and Kagomé layers interconnected with Ba-O and Y-O. For the unit cell of Layer Ⅰ, the stacking of the neighboring Layer Ⅱ follows a translation of (1/3, –1/3, 0) in fractional atomic coordinates. Likewise, the following Layer Ⅲ experiences a subsequent translation of (1/3, –1/3, 0) from Layer Ⅱ, which is (2/3, –2/3, 0) from Layer Ⅰ. Note that these stacking faults are observed in LT-YBCO even after oxygen absorption (Fig. S6a) and after oxygen desorption (Fig. S6b), implying that the post-treatment (such as changes in the atmospheric gases) has limited effects on the stacking faults. Thus, it is concluded that the stacking faults are mainly formed in the synthesis process, *i.e.*, in this case, the phase formation at low firing temperatures. Several researchers have reported that low-temperature syntheses lead to a high probability of the formation of stacking faults in transition metal oxides, such as $Li[Li_{0.2}Ni_{0.2}Mn_{0.6}]O_2$ and Li_2MnO_3.[32–34]

Superlattice formations after oxygen absorption

After oxygen absorption, besides the small particle size and the presence of stacking faults, LT-YBCO exhibits a feature that is different from HT-YBCO in electron diffraction patterns. In the pristine state, distinct spots are observed in SAED patterns viewed along with the $[0\bar{1}10]$ zone axes for both HT- and LT-YBCO (Figs. 3a and 3b, respectively). After oxygen absorption, in addition to the reflections of the parent hexagonal structure (pristine $YBaCo_4O_7$ with the space group of $P6_3mc$), a set of weak and ordered reflections corresponding to structural modulations is observed in HT- and LT-YBCOs. For ease of comparison, the reflections shown here are indexed based on the parent hexagonal structure. With careful examinations, structural modulations (superlattice modulations) in these samples are differentiated. In the oxygenated HT-YBCO (Fig. 3c), as indicated by an arrow, the fundamental diffraction vector of $g_{2\bar{1}\bar{1}2}$ is equally divided into two parts by one satellite spot

(superlattice reflection), in which the superlattice diffraction vector can be described as $g = 1/2g_{2\bar{1}\bar{1}0} + 1/2g_{0002}$. As a result, the superlattice modulation vector is expressed by $q_{o-HC} = 1/2g_{2\bar{1}\bar{1}0} + 1/2g_{0002}$, where o-HC denotes superlattice modulations in the oxygenated HT-YBCO. On the other hand, superlattice reflections in LT-YBCO are modulated at $1/3g_{2\bar{1}\bar{1}0}$, $2/3g_{2\bar{1}\bar{1}0}$, and $1/2g_{0002}$, as indicated by blue (for $1/3g_{2\bar{1}\bar{1}0}$ and $2/3g_{2\bar{1}\bar{1}0}$) and black (for $1/2g_{0002}$) arrows, respectively.

Since no structural modulations are shown in the pristine HT- and LT-YBCOs, the formation of the superstructure is likely irrelevant to the level of crystallinity and the presence of structural defects. Thus, we assume that the superlattice structure might be originated from excess oxygen incorporated in regular positions in the crystal lattice. A similar feature has been reported previously, where the superlattice in association with oxygen nonstoichiometry was found in $YBaCo_4O_{8.1}$,[18] $YBaCo_4O_{8.5}$,[24,35] and $YBaCo_4O_{7.3}$.[36] Moreover, among all the reported oxygen-excess YBCO phases, various types of superlattice are observed, suggesting that the superstructure types depend on the oxygen contents in the crystal lattice. Thus, we assume that the oxygenated HT- and LT-YBCO contain different amounts of oxygen, and hence exhibit dissimilar structural modulations (discussed later). It is noted that the superlattice mostly appears on the {2110} planes. The fact implies that the {2110} planes are the most likely locations for the absorbed oxygen to bond with cobalt under the Kagomé layer, which is in agreement with Jia *et al*.[24]

Electronic structural analysis

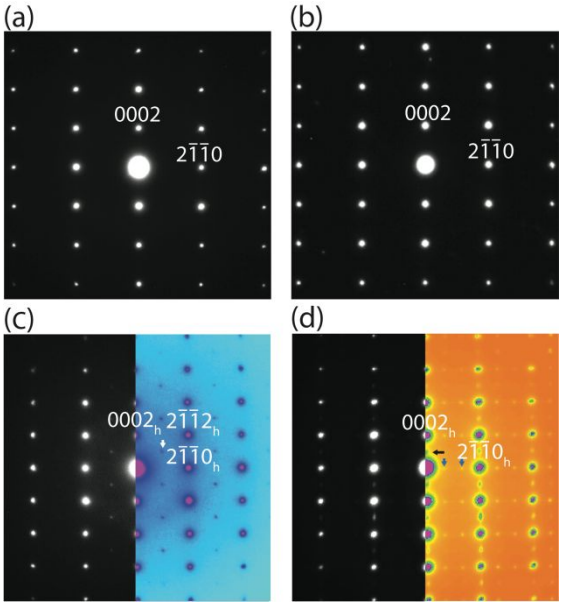

Fig. 3 Selected area electron diffraction (SAED) patterns of pristine (a) HT-YBCO and (b) LT-YBCO taken along the $[0\bar{1}10]$ direction. The SAED patterns of oxygenated (c) HT-YBCO and (d) LT-YBCO viewed along the $[0\bar{1}10]$ direction. The arrow in each image indicates extra spots for structural modulations. Half of the images of (c)(d) are presented in color for ease of viewing.

To gain deeper insights into the differences in the oxygenated phases, electron energy loss spectroscopy (EELS) was used to probe the electronic structures of the YBCO samples. Considering that the prolonged electron beam irradiation gradually leads to sample degradation (*i.e.,* oxygen releases from the crystal lattice), short-time exposure of the electron beam on the sample is necessary to acquire a reliable EEL spectrum, as demonstrated in Fig. S7 (where the spectral features are acquisition time dependent). To be noted, since the Co $L_{2,3}$ and Ba $M_{4,5}$ edges are overlapped, reference spectra are required to identify the Co $L_{2,3}$ and Ba $M_{4,5}$ individually (the reference spectra of $LiCo_2O$, CoO, and $BaCO_3$ were chosen and shown in Fig. S8). Here, we applied EELS measurement on the bulk regions (away from the surface layer) of HT- and LT-YBCOs. In the pristine state (Fig. 4a), the positions of the Co L_3 edge of both HT- and LT-YBCOs are almost the same, located at 777.8 eV and 777.7 eV, respectively. It implies that both samples might have the same cobalt valence, *i.e.*, the ratio of Co^{2+}/Co^{3+} is 3 to 1, because the positions of Co $L_{2,3}$ edge are correlated with the oxidation state of cobalt.[37–39]

Upon oxygen uptake, the Co L_3 position is shifted toward the higher energy loss (778.9 eV and 778.7 eV, for HT- and LT-YBCOs, respectively), while the Ba $M_{4,5}$ position remains unchanged in both samples. Meanwhile, as shown in Fig. 4b, a more pronounced and sharper prepeak appears at 528.9 eV (associated with hybridization of O 2p and Co 3d)[40, 41] in the O K edge, which can be interpreted as the oxidation of cobalt upon oxygen uptake.[37] In other words, excess oxygen atoms are incorporated into the lattice of YBCO and bonded with cobalt ions leading to an increase in the oxidation state of cobalt.[18, 24, 35] For LT-YBCO, a slightly less prominent prepeak is observed (Fig. 4b). A careful examination of the Co L_3 edge reveals an approximately 0.27eV shift to the lower energy loss compared to HT-YBCO. These spectral features are consistent with the fact that LT-YBCO is less oxygenated with a lower Co oxidation state, resulting in the different structural modulations observed in the electron diffraction patterns. It should be emphasized that the EELS results here for the pristine LT-YBCO reveal a different observation from the X-ray absorption near-edge structure and extended X-ray absorption fine structure analysis reported by Chen *et al.*[28] They found that their YBCO sample synthesized at 800 °C possesses a higher amount of extra oxygen with a higher cobalt valence state than those synthesized at 1150 °C.

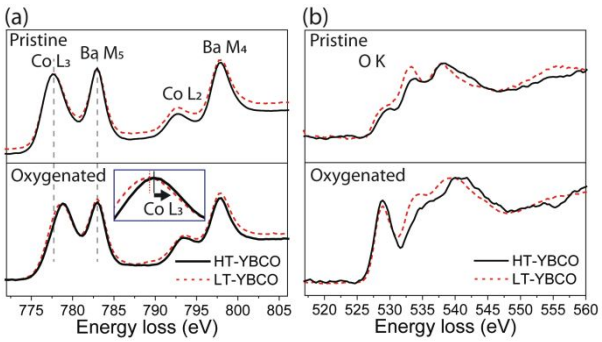

Fig. 4 EEL spectra of (a) Co $L_{2,3}$ Ba $M_{4,5}$, and (b) O K edges for the pristine (top) and oxygenated (bottom) HT- and LT-YBCOs.

Surface structural analysis

To understand the inconsistency between the previous results, we examine the overall structure and find out that the surface structure of LT-YBCO is significantly different from HT-YBCO. Figure 5a presents an annular dark-field (ADF) image taken from the area near the grain surface in LT-YBCO. The EEL spectra of Co $L_{2,3}$, Ba $M_{4,5}$, and O K edges extracted from the horizontal lines 1 (near the surface) to 5 (inner structure) labeled in Fig. 5a are shown in Fig. 5b. First, the Co L_3 edge in the surface spectrum (Line 1) shows a shift of ~0.9 eV to the higher energy loss compared to the inner structure (Line 5), indicating a change in valence states.[38,39,42] In addition, a sharp prepeak around 530 eV is seen in the O K edge of the surface spectrum. The prepeak diminishes in the areas away from the surface (Lines 3 to 5), revealing that the surface has a higher Co oxidation state than the inner structure. For this region, chemical phase maps of Co^{2+}, Co^{3+}, and Co^{2+}/Co^{3+} overlap were extracted using the multiple linear least-squares (MLLS) filling method (Fig. 5a). The spectra of CoO (Co^{2+}), $LiCoO_2$ (Co^{3+}), and $BaCO_3$ (Ba^{2+}) were used as references. The surface (about 40 nm thick) is found to be dominated by Co^{3+} ions, while the inner structure shows the majority of Co^{2+} ions, consistent with the chemical shift in the Co $L_{2,3}$ edge. On the other hand, applying the same method to HT-YBCO indicates no variation in the cobalt valence state (Fig. S9). Thus, the different electronic structures at the surface of LT-YCBO might be related to the smaller particle size or the surface defects incorporated in the crystal lattice.

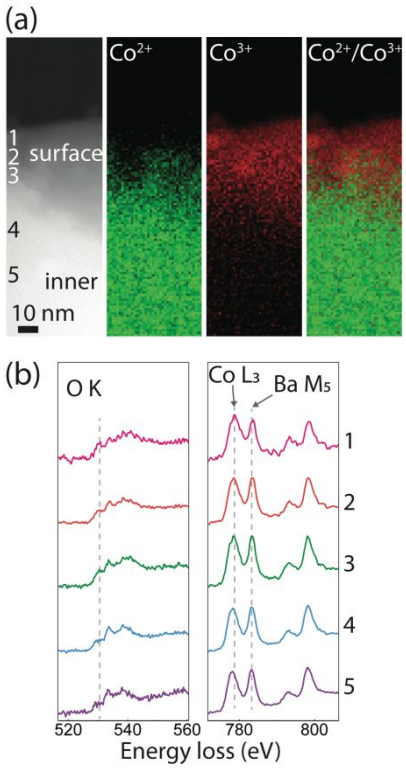

Fig. 5 (a) ADF image of the pristine LT-YBCO particle near the surface and the corresponding MLLS fitting maps of Co^{2+}, Co^{3+}, and Co^{2+}/Co^{3+} overlap, based on the reference spectra of CoO (Co^{2+}), $LiCoO_2$ (Co^{3+}) and $BaCO_3$ (Ba^{2+}). (b) EEL spectra of the O K, Co $L_{2,3}$, and Ba $M_{4,5}$ edges extracted from the horizontal lines 1 to 5 on the ADF image.

In general, the reduction in particle size is accompanied by alternations in its structures and properties. Ma *et al.*[43] observed a reduction in the cobalt oxidation state at the surface (about 3.5 nm thick) of $LaCoO_3$ nanoparticles, which is considerably different from the inner part of the particle, or $LaCoO_3$ thin film.[44] The surface effect becomes prominent in a nanoscale-size particle with a high surface area.[45] In addition, the presence of surface defects possibly modifies the coordinate configuration of cations in the lattice and hence alters the oxidation state.[46] The surface analysis by EELS reasonably explains the discrepancy from the X-ray absorption analysis by Chen *et al.*[28] where the reported higher cobalt valence state of their low-temperature synthesized YBCO would come from the limit of the spatial resolution in the X-ray beam. We suggest that the surface information or the averaging information was detected and contributed to the measured results priorly.

Having found the surface effect on pristine LT-YBCO, the next step is to confirm its influence after oxygen absorption. By means of STEM-EELS followed by MLLS fitting, the electronic states of oxygenated HT-YBCO and LT-YBCO are investigated and shown in Fig. S10 and Fig. S11, respectively. It confirms that the entire particles of both oxygenated HT-YBCO and LT-YBCO are fully oxidized to their equilibrium states. In addition to that, it implies that the pathway of oxygen absorption is not disturbed by the surface effects in LT-YBCO.

Oxygen storage performance

The structural/electronic features caused by the low-temperature synthesis raise questions about possible influences on the oxygen storage performance of LT-YBCO. We performed isothermal thermogravimetry (TG) measurements on HT- and LT-YBCOs at 340 °C upon switching the gas flow from N_2 to O_2 and vice versa. As shown in Fig. 6a, LT-YBCO absorbs oxygen and reaches an equilibrium state in a few minutes at approximately 2.7 wt% (corresponding to the oxygen content of $\delta \sim 0.97$). On the other hand, HT-YBCO does not reach its equilibrium even within 100 min, although this sample can absorb a larger amount of oxygen up to 3.3 wt% (oxygen content of $\delta \sim 1.18$).

According to the EELS analysis discussed earlier, the oxygen content of each sample could be estimated. Assuming that the pristine HT- and LT-YBCOs (in the inner structures) are both oxygen stoichiometric denoted as $YBaCo_4O_7$, the oxygenated HT-YBCO stores excess oxygen of approximately 1.18 per formula unit, which gives the chemical formula of $YBaCo_4O_{8.18}$. Similarly, the chemical formula of the oxygenated LT-YBCO is described as $YBaCo_4O_{7.97}$. However, due to the surface effect in LT-YBCO where the oxygen content is more at the surface as compared to the inner structure, one should consider measuring the overall oxygen content by iodometric titration. As a result, the absolute oxygen content of pristine LT-YBCO was

determined to be 0.12(2), which corresponds to $YBaCo_4O_{7.12}$. Further, accordingly, the oxygenated LT-YBCO should be ascribed as $YBaCo_4O_{8.09}$. In the EELS results, the shift of the Co L_3 edge in HT-YBCO after oxygen uptake is approximately 1.1 eV. Assuming the linear relationship between the energy loss and oxygen content, it gives a gain of δ estimated to be 1.07 per shift in energy loss of 1.0 eV. Since the Co L_3 edge of the oxygenated LT-YBCO is shifted by 1 eV with respect to pristine LT-YBCO in the inner structure without considering the surface effect, yielding an approximately oxygen content of 1.07, in good agreement with the value calculated from the weight changes between the pristine inner-structural and oxygenated LT-YBCO ($\delta_{\text{oxygenated LT-YBCO}} - \delta_{\text{pristine inner-structural LT-YBCO}} \approx 1.09$). It is reminded that the pristine HT-YBCO and LT-YBCO in the inner structure show almost the same peak position of Co L_3 edge as mentioned earlier. It should be noted that the values estimated here are averaged over a large area of the sample. When examining in micrometer or nanometer scale, a local variation in oxygen content would be present depending on the particle size and possibly the defect density.

To further investigate the oxygen uptake/release response and cyclability of the YBCO samples, TG measurements in flowing synthetic air were performed upon temperature swing (Fig. 6b). LT-YBCO can store and release oxygen fully within 10 min. The maximum weight change reaches approximately 2.7 wt%, comparable to the equilibrium value as shown in Fig. 6a, exhibiting excellent reversibility. Even though HT-YBCO stores a larger amount of oxygen up to 3.3 wt% (Fig. 6a), this sample shows relatively slow oxygen uptake/release kinetics to give a smaller weight change in a short period (~2.3 wt%) than LT-YBCO. As expected, with the prolonged time (as with slower heating/cooling rates), HT-YBCO could reach its saturated equilibrium, as shown in Fig. S12. Thus, it is concluded that the improved reaction kinetics of LT-YBCO could be attributed to its smaller particle size and thereby a large specific area for oxygen uptake/release. Similar features regarding the particle size effect on the oxygen absorption/desorption performance of YBCO have also been reported previously.[27]

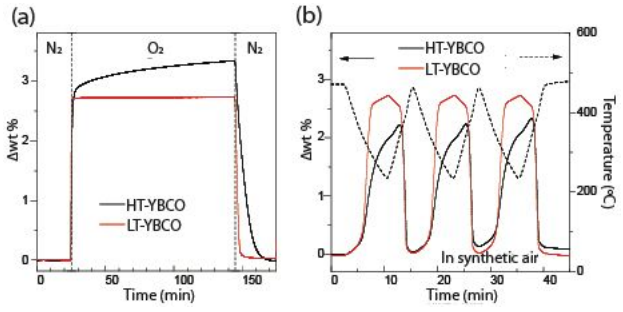

Fig. 6 (a) Isothermal TG curves for HT-YBCO (black) and LT-YBCO (red) measured at 340 °C in the gaseous atmosphere flowing from N_2, O_2, to N_2. (b) TG curves for HT-YBCO (black) and LT-YBCO (red) in flowing synthetic air upon temperature swing between 220 °C and 470 °C. The sample temperature is also shown with a broken curve.

Effects of low-temperature synthesis

Here, the effects of low-temperature synthesis on the microstructures and oxygen storage capacity are discussed. Firing at low temperatures leads to (1) the smaller particle size, (2) the modified electronic structure at the surface, and (3) the formation of stacking faults in the as-prepared LT-YBCO structure. (1) As discussed earlier, the smaller particle size provides large surface areas and increases the density of active sites for oxygen to fill in. Thus, a fast response to oxygen absorption/desorption is expected. This aspect agrees with the literature data, where a high specific surface area gives fast oxygen uptake/release in different types of oxygen storage materials.[47] (2) The variation in electronic structures between the surface and inner regions in pristine LT-YBCO might be attributed to the high defect density at the surface layer of nanometer-sized particles. The presence of atomic defects might affect not only the oxidation state but also the coordination environment of Co cations in the crystal lattice,[45] leading to the modified oxygen storage performance. As reported by Chen *et al*.,[28] high cobalt valence in YBCO particles at the pristine state deteriorates its oxygen storage capacity, in agreement with the findings in our work. (3) The stacking faults are formed during synthesis and distributed randomly along the (0001) planes over the whole grains in LT-YBCO. They remain in the grain even after oxygen absorption. In the oxygenated LT-YBCO, EELS results reveal that it contains Co ions with a lower oxidation state than those in HT-YBCO. Thus, we suggest that the presence of stacking faults suppresses the amount of oxygen that can be stored. On the other hand, the stacking faults may also contribute to the modifications related to oxygen uptake and release, although this is not clear from the present results and will be left as a topic for future investigations. To establish the relationship between structural defect and oxygen storage capacity, comprehensive studies including material synthesis, structural analysis, and theoretical calculations are necessary.

Experimental

Sample preparation

A YBCO sample was synthesized by a complex gel method. $(CH_3COO)_3Y \cdot 4H_2O$ (99.9%, Fujifilm Wako Pure Chemicals), $(CH_3COO)_2Ba$ (99.9%, Fujifilm Wako Pure Chemicals), and $(CH_3COO)_2Co \cdot 4H_2O$ (99.9%, Fujifilm Wako Pure Chemicals) were used as starting reagents. A stoichiometric amount of these reagents were dissolved in Milli-Q water in which equimolar citric acid (Fujifilm Wako Pure Chemicals) was subsequently added as a complexing agent. The citrate solution was mixed with an ammonia solution while the pH was adjusted to ~7. The solution was heated at about 70 °C and stirred until a gelatinous product was formed. The resultant product was calcined at 600 °C in air for 1 h, thoroughly ground, and again prefired at 6 h to remove organic residues. The resultant precursor was again ground, pelletized, and fired at 800 °C for 12 h in flowing N_2 gas (99.99%).

A YBCO sample by the conventional synthesis route was also prepared as a reference. Y_2O_3 (99.99%, Fujifilm Wako Pure Chemicals), $BaCO_3$ (99.9%, Fujifilm Wako Pure Chemicals), and Co_3O_4 (99.9%, Kojundo Chemical Laboratory Co., Ltd.) were used as starting reagents. A stoichiometric amount of these reagents were thoroughly mixed, pelletized, and fired at 1200 °C for 24 h in air, followed by rapid cooling to room temperature.

Structural analysis

The phase purity and the lattice constants of the samples were checked by X-ray powder diffraction (XRD; Ultima IV Protectus, Rigaku; Cu Kα radiation). The measurements were performed in an angular range of 10 – 90° with a step size of 0.02° and a scan rate of 5° min^{-1}.

For surface analysis by electron energy loss spectroscopy (EELS), the specimens were prepared by distributing YBCO particles on a holey carbon film support on a copper grid. For internal structure observation, to avoid the effects of surface states, the particles were embedded in epoxy resin (G2, Gatan, Inc.) and then wedge-polished to obtain a sliced particle sample. The thinning process after wedge polishing was performed using Ar-ion milling (PIPS Ⅱ, Gatan, Inc.) with a cold stage. Except for Fig. 5, Fig. S9, Fig S10 and Fig. S11, images were taken from sliced particle samples made by wedge-polishing.

Scanning transmission electron microscopy (STEM) images and electron diffraction patterns were taken by an aberration-corrected (CEOS GmbH) STEM (JEM-2400FCS, JEOL Ltd.), operating at an accelerating voltage of 200 kV. The collection angles of 68-280 mrad were set for high-angle annular dark-field STEM (HAADF-STEM) imaging. The probe-forming aperture with a semiangle of 22 mrad was used. To improve the signal-to-noise ratio while minimizing the sample damage, we used a beam current of 2.4 pA and a pixel dwell time of 5 μs to collect a series of images and then integrate them. To evaluate the oxidation state of cobalt, a Wien filter monochromated aberration-corrected STEM (JEM-2400FCS, JEOL Ltd.) equipped with an electron energy loss spectroscope (EELS, GIF Continuum ER, Gatan, Inc.) was utilized. EEL spectra were recorded in the STEM mode using a 0.3 eV per channel with an energy resolution (full-width at half-maximum of zero-loss peak) of 0.9 eV. Each spectrum was then background subtracted and deconvoluted using the corresponding zero-loss spectrum to remove the multiple inelastic scattering effects, operated in Gatan Microscopy Suite software (GMS3.4).

Thermogravimetric measurement

The oxygen uptake/release characteristics of the samples were investigated employing thermogravimetry (TG; Thermo Plus Evo TG-8120, Rigaku). Approximately 30 mg of a YBCO powder was used. Prior to the measurements, the sample was rapidly heated to 500 °C and then cooled in flowing N_2 gas to remove excess oxygen in the crystal lattice. Isothermal TG experiments were performed at 340 °C upon switching the gas flow from N_2 to O_2 and vice versa. The oxygen concentration in N_2 gas is approximately 10 to 20 ppm. The sample weight was also measured in synthetic air (21% O_2 + 79% N_2) upon temperature swing between 220 °C and 470 °C.

Conclusions

In summary, we gained some insights into the crystal structures and electronic structures of $YBaCo_4O_{7+\delta}$ (YBCO) materials synthesized at low temperatures. Different from the conventional synthesis temperatures of 1200 °C, low temperature firing at approximately 800 °C significantly reduces the particle size and, therefore, enhances the response to oxygen absorption/desorption (one cycle completed within 10 min). Meanwhile, a high cobalt valence state is observed at the surface of the particle, which is different from the inner structure, suggesting to be driven by the reduction in particle size. In addition, stacking faults are found randomly distributed. The presence of stacking faults is believed to have an impact on oxygen storage performance. For the oxygenated phases, both LT- and HT- YBCOs involve superlattices caused by excess oxygen atoms absorbed in the YBCO lattice, indicating that the formation of superlattices is irrelevant to stacking faults. This work justifies the need for additional spectroscopic experiments together with theoretical calculations to better understand the nature of the stacking faults and surface structure. Further, in light of interesting features found in the study of the defects/superlattice and tunable oxygen storage properties, this structure is expected to not only widen its potential use in diverse applications but also offer a blueprint to other complex metal oxides.

Conflicts of interest

There are no conflicts to declare.

Acknowledgements

This work was supported in part by JSPS KAKENHI Grant Numbers JP 18K04840, JP 21K18196 and JP 22H04914 also by Council for Science, Technology and Innovation (CSTI), Cross-ministerial Strategic Innovation Promotion Program (SIP), “Energy systems towards a decarbonized society” (Funding agency: JST).

References

1 J. Kašpar, P. Fornasiero and M. Graziani, *Catal. Today* 1999, **50**, 285-298.
2 N. Guilhaume and M. Primet, *J. Catal.* 1997, **165**, 197-204.
3 J.-H. Kim and A. Manthiram, *Chem. Mater.* 2010, **22**, 822-831.
4 S.A. Ghom, C. Zamani, S. Nazarpour, T. Andreu and J.R. Morante *Sens. Actuators B Chem.* 2009, **140**, 216-221.
5 Z. Yang, Y.S. Lin and Y. Zeng, *Ind. Eng. Chem. Res.* 2002, **41**, 2775-2784.
6 T. Motohashi, T. Ueda, Y. Masubuchi, M. Takiguchi, T. Setoyama, K. Oshima and S. Kikkawa, *Chem. Mater.* 2010, **22**, 3192-3196.
7 O. Parkkima and M. Karppinen, *Eur. J. Inorg. Chem.* 2014, **2014**, 4056-4067.

8 T. Motohashi, S. Kadota, H. Fjellvåg, M. Karppinen and H. Yamauchi, *Mater. Sci. Eng.: B* 2008, **148**, 196-198.
9 Y. Nagai, T. Yamamoto, T. Tanaka, S. Yoshida, T. Nonaka, T. Okamoto, A. Suda and M. Sugiura, *Catal. Today* 2002, **74**, 225-234.
10 M. Karppinen, H. Yamauchi, S. Otani, T. Fujita, T. Motohashi, Y.H. Huang, M. Valkeapää and H. Fjellvåg, *Chem. Mater.* 2006, **18**, 490-494.
11 S. Räsänen, H. Yamauchi and M. Karppinen, *Chem. Lett.* 2008, **36**, 638-639.
12 T. Komiyama, T. Motohashi, T. Masubuchi and S. Kikkawa, *Mater. Res. Bull.* 2010, **45**, 1527-1532.
13 M. Valldor and M. Andersson, *Solid State Sci.* 2002, **4**, 923-931.
14 M. Valldor, *Solid State Sci.* 2004, **6**, 251-266.
15 V. Caignaert, A. Maignan, V. Pralong, S. Hébert and D. Pelloquin, *Solid State Sci.* 2006, **8**, 1160-1163.
16 L.C. Chapon, P.G. Radaelli, H. Zheng and J.F. Mitchell, *Phys. Rev. B* 2006, **74**, 172401.
17 A. Huq, J.F. Mitchell, H. Zheng, L.C. Chapon, P.G. Radaelli, K.S. Knight and P.W. Stephens, *J. Solid State Chem.* 2006, **179**, 1136-1145.
18 O. Chmaissem, H. Zheng, A. Huq, P.W. Stephens and J.F. Mitchell, *J. Solid State Chem.* 2008, **181**, 664-672.
19 N.V. Podberezskaya, N.B. Bolotina, V.Y. Komarov, M.Y. Kameneva, L.P. Kozeeva, A.N. Lavrov and A.I. Smolentsev, *Crystallogr. Rep.* 2015, **60**, 484-492.
20 S.R.W. Johnston, B. Ray, W. Hu and I.S. Metcalfe, *Solid State Ion.* 2018, **320**, 292-296.
21 M. Xu, I. Ermanoski, E.B. Stechel and S. Deng, *Chem. Eng. J.* 2020, **389**, 124026.
22 B. Wang, J. Wang, A. Chang and J. Yao, *RSC Adv.* 2019, **9**, 25488-25495.
23 C. Zhou, P. Xie, Y. Chen, Y. Fan, Y. Tan and X. Zhang, *Ceram. Int.* 2015, **41**, 4696-4705.
24 Y. Jia, H. Jiang, M. Valkeapää, R. Dai, H. Yamauchi, M. Karppinen and E.I. Kauppinen, *Solid State Ion.* 2011, **204-205**, 7-12.
25 R. Samuli, Y. Hisao and K. Maarit, *Chem. Lett.* 2008, **37**, 638-639.
26 E.A. Juarez-Arellano, M. Kakazey, M. Vlasova, G. Urquiza-Beltran, M. Aguilar-Franco, X. Bokimi, E. Martinez and E. Orozco, *J. Alloys Compd.* 2010, **492**, 368-372.
27 T. Chen, Y. Asakura, T. Hasegawa, T. Motohashi and S. Yin, *J. Mater. Sci. Technol.* 2021, **68**, 8-15.
28 T. Chen, T. Hasegawa, Y. Asakura, M. Kakihana, T. Motohashi and S. Yin, *ACS Appl. Mater. Interfaces* 2021, **13**, 51008-51017.
29 S.J. Pennycook and L.A. Boatner, *Nature* 1988, **336**, 565-567.
30 S.J. Pennycook and P.D. Nellist, *Scanning Transmission Electron Microscopy*. Springer: New York, NY, 2011.
31 K. Momma and F. Izumi, *J. Appl. Crystallogr.* 2011, **44**, 1272-1276.
32 R. Shunmugasundaram, R.S. Arumugam and J.R. Dahn, *J. Electrochem. Soc.* 2016, **163**, A1394-A1400.
33 D.Y.W. Yu, K. Yanagida, Y. Kato, and H. Nakamura, *J. Electrochem. Soc.* 2009, **156**, A417.
34 T. Matsunaga, H. Komatsu, K. Shimoda, T. Minato, M. Yonemura, T. Kamiyama, S. Kobayashi, T. Kato, T. Hirayama, Y. Ikuhara, H. Arai, Y. Ukyo, Y. Uchimoto and Z. Ogumi, *Chem. Mater.* 2016, **28**, 4143-4150.
35 Y. Jia, H. Jiang, M. Valkeapää, H. Yamauchi, M. Karppinen and E.I. Kauppinen, *J. Am. Chem. Soc.* 2009, **131**, 4880-4883.
36 M.A. Kirsanova, V.D. Okatenko, D.A. Aksyonov, R.P. Forslund, J.T. Mefford, K.J. Stevenson and A.M. Abakumov, *J. Mater. Chem. A* 2019, **7**, 330-341.
37 Y. Zhao, T.E. Feltes, J.R. Regalbuto, R.J. Meyer and R.F. Klie, *J. Appl. Phys.* 2010, **108**, 063704.
38 L.A.J. Garvie, A.J. Craven and R. Brydson, *Am. Mineral.* 1994, **79**, 411-425.
39 T.-H. Shen, L. Spillane, J. Vavra, T.H.M. Pham, J. Peng, Y. Shao-Horn and V. Tileli, *J. Am. Chem. Soc.* 2020, **142**, 15876-15883.
40 F.M.F. de Groot, M. Abbate, J.van Elp, G.A. Sawatzky, Y.J. Ma, C.T. Chen and F. Sette, *J. Phys. Condens. Matter* 1993, **5**, 2277-2288.
41 F.M.F. de Groot, *J. Electron Spectrosc. Relat. Phenom.* 1993, **62**, 111-130.
42 Y. Zhao, T.E. Feltes, J.R. Regalbuto, R.J. Meyer and R.F. Klie, *J. Appl. Phys.* 2010, **108**, 063704.
43 C. Ma, N. Lin, Z. Wang, S. Zhou, H. Yu, J. Lu and H. Huang, *Phys. Rev. B* 2019, **99**, 115401.
44 J.-H. Kwon, W.S. Choi, Y.-K. Kwon, R. Jung, J.-M. Zuo, H.N. Lee and M. Kim, *Chem. Mater.* 2014, **26**, 2496-2501.
45 Z. Zhang, *Ultramicroscopy* 2007, **107**, 598-603.
46 X. Hao, A. Yoko, K. Inoue, Y. Xu, M. Saito, C. Chen, G. Seong, T. Tomai, S. Takami, A.L. Shluger, B. Xu, T. Adschiri and Y. Ikuhara, *Acta Mater.* 2021, **203**, 116473.
47 Q. Liang, X. Wu, X. Wu and D. Weng, *Catal. Lett.* 2007, **119 (3)**, 265-270.

